Understanding the interplay of capillary and viscous forces in CO2 core flooding experiments

Citation for published version:
Jin, X, Chao, C, Edlmann, K & Fan, X 2022, 'Understanding the interplay of capillary and viscous forces in CO2 core flooding experiments', *Journal of Hydrology*, vol. 606, 127411.
https://doi.org/10.1016/j.jhydrol.2021.127411

Digital Object Identifier (DOI):
10.1016/j.jhydrol.2021.127411

Understanding the interplay of capillary and viscous forces in CO_2 core flooding experiments

Xiaoqiang Jin[a], Cong Chao[a], Katriona Edlmann[b], Xianfeng Fan[a, *]

a Institute for Materials and Processes, School of Engineering, The University of Edinburgh, Edinburgh, EH9 3JL, UK

b School of Geosciences, University of Edinburgh, Edinburgh EH9 3FE, UK

*Corresponding author: x.fan@ed.ac.uk

Abstract

Interaction between capillary and viscous forces significantly affects the flow instability in immiscible displacement, which is usually investigated by visualization of flow patterns in 2d porous micromodels or in 3d system equipped with X-ray CT. However, in most practical applications, visualization of flow in porous media is not possible and the pressure signal is often as one of the important sources of information. Core flooding experiments were implemented in this study to investigate the interplay of capillary and viscous effects by analysis of differential pressure. Water and crude oil were employed as defending fluid, and different states of CO_2 were injected as invading fluid. The inlet was set as the constant injection flow rate while the outlet as the constant pressure. In viscous-dominated displacement, differential pressure evidently depends on the injection rate and the pressure decline curve is fitted by a power function. The exponent of the function is found to be significantly larger at the crossover between capillary-dominated and viscous-dominated regions. In capillary-dominated displacement, the pressure profile is characterized by a pressure jump at the beginning and intermittent fluctuations during displacement. Further analysis by wavelet decomposition indicates a transition point existing in standard deviation of pressure fluctuations when the displacement is transformed from capillary-dominated to viscous-dominated. The experiment results are finally verified by a macroscopic capillary number, which characterizes the interaction between capillary and viscous forces at a critical value of $N_{ca}^{macro} \sim 1$, agreeing well with the Log Nca-Log M phase diagram.

Keywords: CO_2 storage; CO_2 enhanced oil recovery; capillary force; viscous force; differential pressure; macroscopic capillary number.

1. Introduction

Immiscible displacement in porous media is important in many applications of subsurface transports, including CO_2 sequestration, enhanced oil recovery (EOR) and removal of nonaqueous phase liquids (NAPLs) (Khudaida and Das, 2020; Li and Yu, 2020; Singh et al., 2019b; Zhou et al., 2020). The process where a nonwetting phase invades into the permeable media and displaces the wetting phase is named as drainage. The instability in drainage process arises when a fluid displaces a more viscous fluid. Dynamics of instability is governed by the competition between viscous and capillary effects (Weitz et al., 1987). Fingering is usually encountered in unstable displacement and is one of the major reasons for the poor efficiency of recovery or remediation processes (Zhao et al., 2016).

During drainage, non-wetting phase invades the pore space with a series of cooperative pore filling events, such as burst (Haines jump), touch and overlap events, on the microscale (Cieplak and Robbins, 1990; Holtzman and Segre, 2015; Primkulov et al., 2019). The process is significantly affected by viscosity of fluids, interfacial tension, pore wettability, flowrate of invading phase, heterogeneity of pore structure, etc (Abidoye and Das, 2020; Goel et al., 2016). Lenormand et al. (1988) characterized these effects into two dimensionless numbers, the capillary number (Nca), which is the ratio of viscous forces to capillary forces, and the viscosity ratio (*M*), which is the ratio of invading to defending fluid viscosities. Different flow patterns, defined as capillary fingering, viscosity fingering and stable displacement, were observed when the displacement processes were dominated either by capillary or viscous forces. Lenormand et al. (1988) proposed a log *Nca*-log *M* phase diagram consisted of three domains, corresponding to three different flow patterns and displacement mechanisms, based on the value of *Nca* and *M*. Though the boundaries of the domains in the diagram are affected by variation of pore size or pore distribution of networks, the general shape of the diagram remains unchanged (Tsuji et al., 2016). A similar phase diagram was obtained by Zhang et al. (2011) and the crossover regions between each of three domains were noticeably smaller than Lenormand's by using a precision-fabricated micromodel with smaller pore throats (about 40 μm). Chen et al. (2017) proposed a phase diagram for the displacement patterns in a rough fracture and the crossover region from capillary to viscous fingering is narrower than that in Lenormand's and Zhang's results due to the different flow geometry and smaller tortuosity in rough fractures. The phase diagram has also been confirmed by two-dimensional pore-scale simulations either in uniform porous medium or random porous media networks (Amiri and Hamouda, 2014; Leclaire et al., 2017). In addition, the phase diagram has been approved to be applicable to 3-D conditions by many 3-D simulations with natural sandstone (Leclaire et al., 2017; Tsuji et al., 2016; Yamabe et al., 2015) and experiment with glass beads model (Hu et al., 2020; Patmonoaji et al., 2020). Tsuji et al. (2016) compared the differences between two-phase flow in 3D natural rock and that in 2D homogeneous models by two-phase lattice Boltzmann simulations. The results revealed that the log *Nca*-log *M* diagram for 3D natural rock and for 2D homogeneous network are similar except the onset of capillary fingering in 3D natural rock at higher Ca than that in 2D homogeneous models. The simulation results are in accord with a recent 3-D glass beads porous media experiment (Hu et al., 2020), which also demonstrated that rough location of three displacement patterns on the log *Nca*-log *M* diagrams was consistent with previous studies in 2D micromodel. Besides phase diagram, fractal analysis by the box-counting method to distinguish the displacement patterns, has been employed extensively to study the transition from capillary invasion to viscous fingering. By controlling the wettability of the invading fluid, Zhao et al. (2016) observed a transition from capillary fingering ($D_f \approx 1.82$) to viscous fingering ($D_f \approx 1.62$) when *Nca* increases in strong drainage in a two-dimensional microfluidic flow cell, which is consistent with the results from Måløy et al. (1985). Both phase diagram and fractal analysis require the direct visualization of displacement patterns and most of experiments are restricted in a two-dimensional porous media network.

However, visualization of flow in porous media in most practical applications is not possible and resolving the dynamics of pore-scale processes by 3D imaging techniques like X-ray computed tomography (CT) is still a demanding task, which involves expensive equipment and time-consuming data acquisition methods (Berejnov et al., 2010; Singh et al., 2019b). The pressure signal is often as one of the important sources of information. Primkulov et al. (2019) developed a 'moving capacitor' dynamic network model to study the relationship between displacement patterns and pressure signals and the results indicated that it is possible to infer the characteristics of the displacement purely from the pressure signals. In drainage with high Nca, the pressure gradient is maintained mainly by viscous defending fluid and it decreases gradually when defending fluid is displaced (Zhao et al., 2016). In slow capillary-dominated displacement, pressure field is virtually uniform in each fluid, and it displays typical intermittent fluctuations in pressure signals (Knudsen and Hansen, 2002; Zacharoudiou et al., 2018). The fluctuations consisting of discrete negative pressure jumps, which are identified as Haines jumps, have been observed both in experiments and simulations (Aker et al., 2000; Furuberg et al., 1996). They are the result of bursts of fluid-fluid interfaces by making a sudden and fast jump through the throat to the adjacent pores, then halting at the next throat which has a higher threshold pressure (Singh et al., 2019a). This burst-like invasion was found to be favourable for displacement efficiency in slow drainage while wetting films on the solid surfaces dominates the imbibition with high Nca, leading to incompact displacement (Zhao et al., 2016).

Though numerous works have studied the interplay between capillary force and viscous force in fluid-fluid displacement through phase diagram, fractal analysis and pressure signals, most of them are limited to simulations and two-dimensional porous media network experiments. In this study, CO_2-water and CO_2-crude oil core flooding experiments are conducted respectively under various in-situ conditions. Based on the log Nca-log M phase diagram, the displacements are characterized by different mechanisms. The behaviours of differential pressure are first compared in displacements dominated by different mechanisms. By using wavelet decomposition analysis of pressure fluctuations, the interplay between capillary and viscous effects is quantified from a pore-scale perspective. The experiment results are finally verified by a macroscopic capillary number.

2. Materials and experimental setup

2.1 Materials and their properties

Drainage experiments with various capillary numbers and viscosity ratios were conducted by employing deionized water (DI water) and viscous crude oil as defending fluids and different states of CO_2 as invading fluids. DI water with an electrical resistivity greater than 18.18 MΩ·cm was used. Crude oil was obtained from BP Exploration Operating Co Ltd with a specific gravity of 0.837 at 20 °C. The viscosity of the crude oil was measured by a Haake Mars rheometer (Thermo Scientific, Germany) with a plate-plate system (diameter, 60 mm) and the measurement was performed at shear rates from 50 to 1000 s^{-1} with temperature increasing from 25 to 80 °C, as shown in Fig. 1(a). The independence of viscosity on shear rate shows the crude oil is a Newtonian fluid in the temperature range (George and Qureshi, 2013). The viscosity decreases obviously with the increase of temperature and the relationship is well fitted by the Arrhenius equation ($\eta(T) = \eta(T_0)exp\left[\frac{E_a}{R}(\frac{1}{T} - \frac{1}{T_0})\right]$, where $\eta(T)$ is viscosity at temperature T (K), $\eta(T_0)$ viscosity at temperature T_0 (K), R is universal gas constant (J·mol^{-1}·K^{-1}), E_a is activation energy (J/mol)) in Fig. 1(b) (Messaadi et al., 2015). Dry CO_2 was supplied by BOC with a guaranteed minimum purity level 99.995% in a cylinder fitted with a dip tube to permit withdrawal of liquid phase of CO_2. The viscosities of water and CO_2 are available from NIST CHEMISTRY Webbook website (Chase Jr and Tables, 1998). The values of interfacial tension (IFT) between CO_2 and water are obtained from Bachu's experiment data (Bachu and Bennion, 2008). Interfacial tension between CO_2 and crude oil is estimated by Baker-Swerdloff method, which first obtains the interfacial tension value at atmosphere pressure based on API gravity and temperature, and then represents the effect of CO_2 dissolution in crude oil at greater pressures by a graphical correction factor (Abdul-Majeed and Al-Soof, 2000). Physical properties of the six fluid pairs used in each displacement experiments are summarized in Table 1.

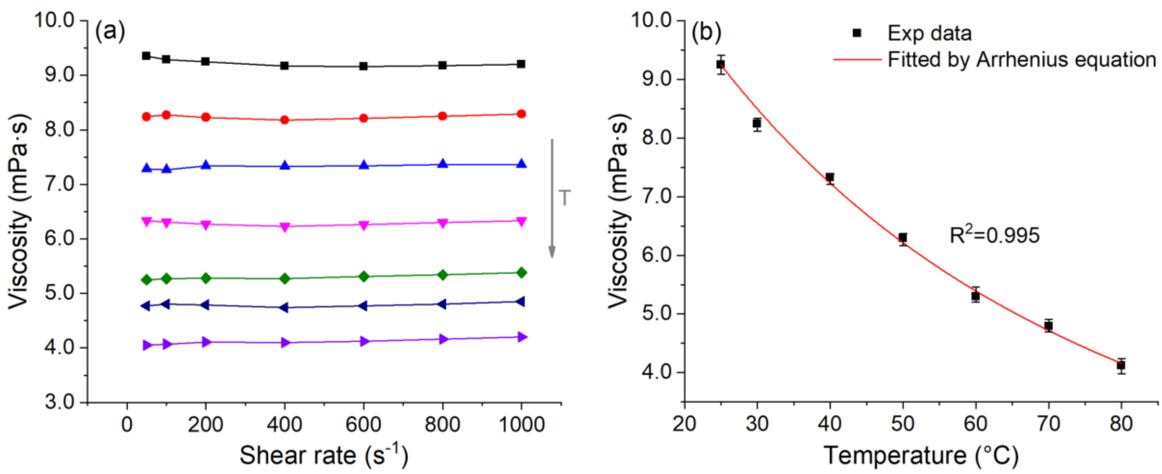

Fig. 1 (a) Relationship between crude oil viscosity and shear rate with temperature increasing from 25 to 80 °C, (b) Dependence of crude oil viscosity on temperature and fitted by Arrhenius equation (Messaadi et al., 2015).

Table 1 Summary of experimental conditions and physical properties of defending and invading fluids.

T (°C)	P (bar)	Defending fluid	Invading fluid	Viscosity (mPa·s)		Log M	IFT (mN/m)
				μ_d	μ_i		
17	45	water	gCO_2	1.077	0.016	-1.828	40.4
40	80	water	sCO_2	0.654	0.023	-1.454	31.3
22	80	water	LCO_2	0.952	0.072	-1.121	29.8
23	45	crude oil	gCO_2	9.576	0.016	-2.777	16.4
40	80	crude oil	sCO_2	7.233	0.023	-2.498	9.9
23	80	crude oil	LCO_2	9.576	0.070	-2.136	10.7

2.2 Core sample

The reservoir core sample was provided by Anasuria Operating Company, UK, with a diameter of 2.3 cm, a length of 3.7 cm, an average porosity of 0.23 and a pore volume (PV) of 3.5 cm^3. The absolute water permeability of the core sample was measured as 129 mD at confining pressure of 138 bar (2000 PSI). The core sample is oil-wet and intermediate water-wet in air, as shown in Fig. S1. The pore size distribution measurement was performed by an Autopore IV 9500 mercury injection porosimeter (Micromeritics, USA), as shown in Fig. 2. It can be seen most pore throats are in the range of 1.0 to 30.0 μm and median pore diameter calculated with volume and 4V/A algorithms are around 13.1 μm and 5.2 μm, respectively.

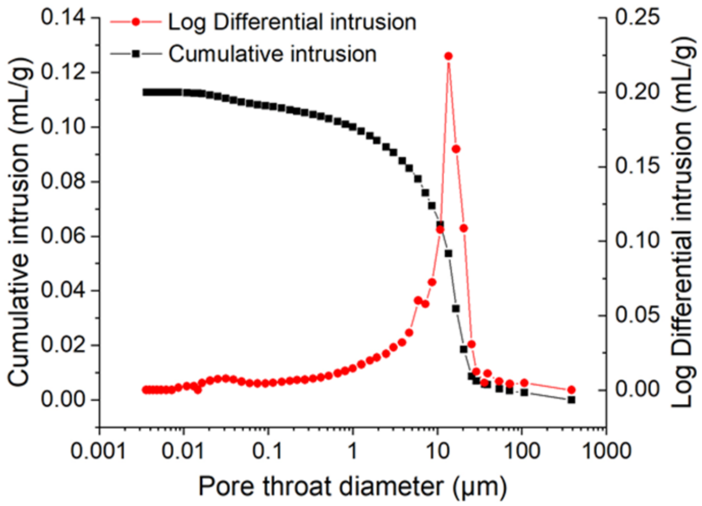

Fig. 2 Pore size distribution of the core sample determined by mercury injection porosimeter. Cumulative mercury intrusion and Log differential mercury intrusion as a function of pore throat size, showing median pore diameter around 13.1 μm.

The sandstone is originated from the Upper Jurassic fulmar sands of the North Sea Guillemot oil field, deposited within a subsiding shallow marine basin as a sequence of shallow marine and deep-water submarine fans (Banner et al., 1992; Johnson et al., 1986). In thin section (Fig. 3), the sandstone is primarily composed of fine grained, sub angular well-sorted quartz grains (~70%) and feldspar (~27%). Most of the porosity is intergranular with notable intergranular porosity because of the dissolution of the albite, microcline, and orthoclase feldspars. The bulk composition of the sandstone has been determined by X-Ray diffraction using a D8 Advance (Bruker, USA) equipped with an energy dispersive detector (Sol-X), as shown in Fig. 4. Three samples are measured to ensure representativity of the results. The results for all samples can be seen in Table 2 and confirm that the dominant mineralogy is Quartz (~70 wt.%) with ~14.4 wt.% Albite, ~6.3 wt.% Microcline and ~5.7 wt.% Orthoclase and minor (less than 1 wt.%) Muscovite, Illite and Pyrite. Among these minerals, CO_2-water contact angle on quartz, feldspar and calcite do not have significant change versus pressure while the water wettability of muscovite mica changed from strongly water-wet to intermediate water-wet with increasing pressure (Farokhpoor et al., 2013). Due to the small amount of Muscovite (0.72 wt.%) in the sample, its effect on contact angle can be considered insignificant.

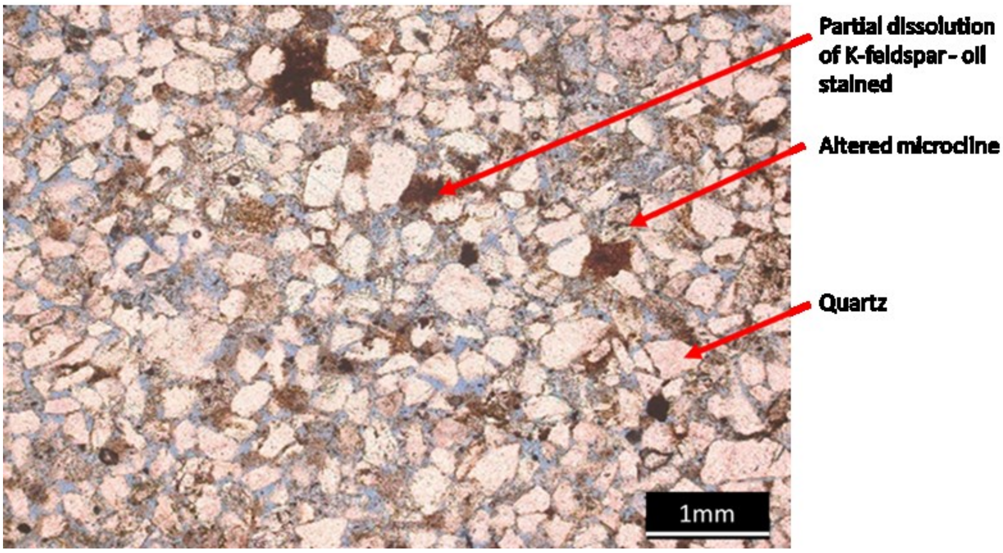

Fig. 3 Optical microscope thin section view of the sandstone (blue stained areas are porosity).

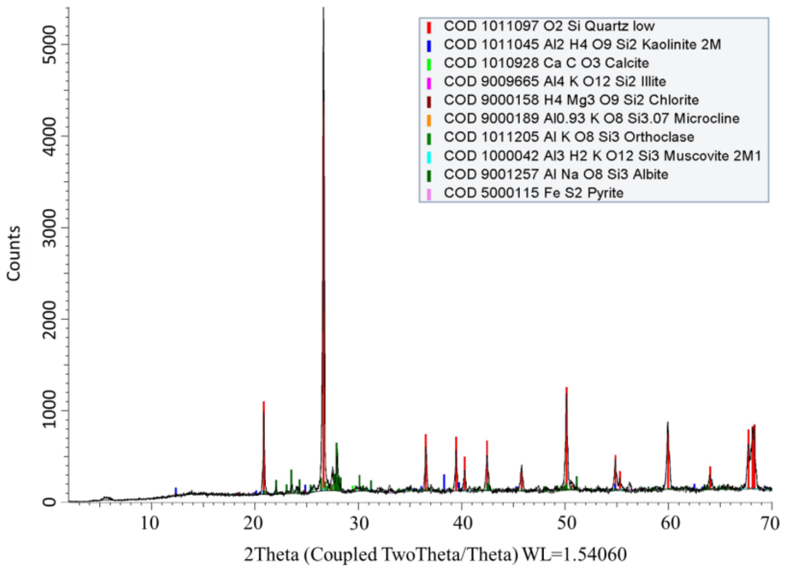

Fig. 4 X-ray diffractograms for mineral analysis of the core sample.

Table 2 results from the XRD analysis of the sample.

Mineral	Chemical Formula	Mineral weight percent (%) Sample 1	Mineral weight percent (%) Sample 2	Mineral weight percent (%) Sample 3	Average mineral weight percent (%)
Quartz	SiO_2	70.50	72.33	69.40	70.74
Corundum	Al_2O_3	0.34	0.31	0.33	0.33
Calcite	$CaCO_3$	0.00	0.04	0.15	0.06
Pyrite	FeS_2	0.15	1.40	0.24	0.60
Albite	$NaCaAlSi_3O$	15.32	13.11	14.91	14.45
Gypsum	$CaSO_4$ $2H_2O$	0.72	0.00	0.27	0.33
Illite	$(K)(Al,Mg,Fe)_2(Si,Al)_4O_{10}$	0.00	0.69	1.28	0.66
Kaolinite	$Al_2Si_2O_5(OH)_4$	0.00	0.00	0.00	0.00
Chlorite	$(Mg,Fe)_3(Si,Al)_4O_{10}(OH)_2$	0.05	0.08	0.05	0.06
Microcline	$KAlSi_3O_8$	6.57	6.09	6.32	6.33
Orthoclase	$KAlSi_3O_8$	6.16	5.19	5.75	5.70
Muscovite	$KAl_2(AlSi_3O_{10})(F,OH)_2$	0.15	0.76	1.25	0.72

2.3 Experiment procedures

Drainage experiments were conducted under different reservoir conditions where CO_2 can be injected in different states. The experiment system is shown in Fig. 5. The core sample was wrapped in a shrinkable rubber sleeve and placed in the horizontal core holder by neglecting the effect of gravity. The confining pressure of 138 bar was built by the overburden pressure pump (Milton Roy, CM4000) and was always larger than the pore pressure, which ensures the compact contact between the core sample and sleeve to prevent the flow from bypassing the core sample. Prior to displacement experiments, the core holder was immersed in hot water bath (Grant Instruments, GD100) for 6 hours to reach thermal equilibrium and then at least 30 pore volumes of defending fluid were injected by water/oil pump (ISCO syringe pump, 100DM) into the core sample at a high injection rate of 20 mL/min to remove the gas in the system and to make the core sample fully saturated (line 1 and 3 open, line 2 and 4 closed). After back pressure was built by injecting defending fluid into the outlet of the core sample by water/oil pump, CO_2 was injected into the core sample by CO_2 pump at a constant injection rate (line 2 and 4 open, line 1 and 3 closed). During the drainage process, the transient data of inlet pressure, outlet pressure and effluent production was monitored. The inlet and outlet pressures were measured by pressure transducers and automatically recorded every 6 seconds by LabVIEW. The cumulative production of effluents was recorded very minute. Every displacement was ceased after injecting 2 pore volume of CO_2 and the core sample was taken out to be weighed by a Sartorius scale with a resolution of 0.0001 g after experiment. CO_2 breakthrough time was determined through replacing the water/oil pump by a back-pressure valve (line 3 and 4 open, line 1 and 2 closed).

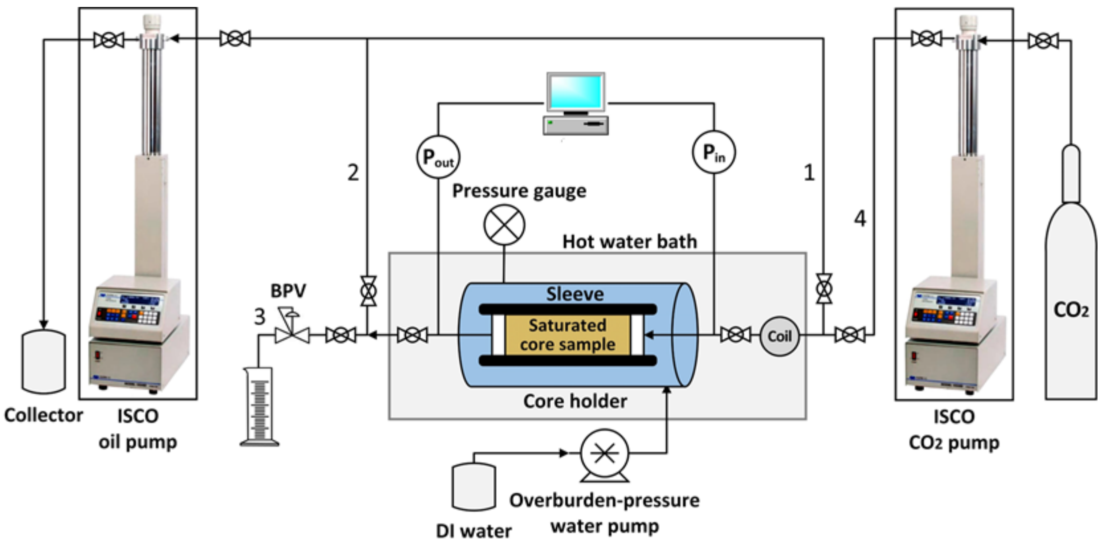

Fig. 5 Schematic diagram of CO_2 core flooding system.

3. Results and discussions

The interplay between viscous and capillary force in immiscible displacement is related to viscosity of fluids, interfacial tension, wettability of fluids and pore surfaces, flowrate of invading phase, heterogeneity of pore structure, etc., which has been characterized into two dimensionless numbers *Nca* and *M* (Lenormand et al., 1988),

$$Nca = \frac{\mu_d v}{\sigma} = \frac{\mu_d Q}{\sigma A} \quad (1)$$

$$M = \frac{\mu_i}{\mu_d} \quad (2)$$

where σ is the interfacial tension, v is superficial velocity, Q is the injection flowrate, A is the cross section area of the core sample, μ_i and μ_d are viscosity of invading and defending fluid, respectively. Variation of Nca was achieved by increasing the injection flowrate and variation of M was obtained by injecting different phases of CO_2 and by employing water and crude oil as defending fluid respectively. The values of Log *Nca* are summarized in Table 3 as a function of injection rate. The log *Nca*-log *M* phase diagram composed of three displacement patterns is shown in Fig. 6 and the experiment conditions are included in the figure. Crossover areas exist between different displacement modes and the boundaries depends on the system, especially on the geometry of the porous media (Lenormand et al., 1988; Yamabe et al., 2015; Zhang et al., 2011).

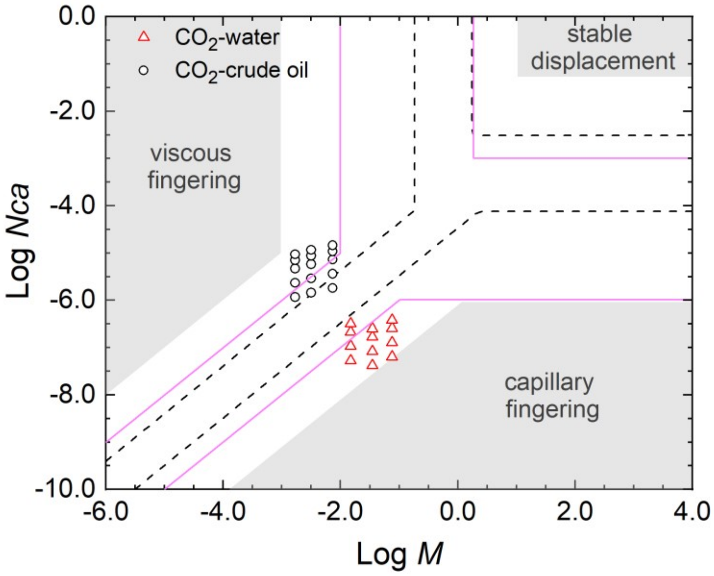

Fig. 6 Log *Nca*-Log *M* phase diagram showing three displacement mechanisms and their boundaries. The grey boundaries proposed by Lenormand's numerical model with pore throats around 230 μm (Lenormand et al., 1988) ,boundaries of dash black lines indicated by Zhang's 2D micromodel experiment results with pore throats about 40 μm (Zhang et al., 2011) and boundaries of purple solid line obtained by Hu's 3D glass beads porous media model with pore throats around 100 μm (Hu et al., 2020). The experiment conditions denoted by black circles and red rectangles standing for CO_2-crude oil and CO_2-water flooding, respectively.

Though the phase diagram is applicable both to 2D and 3D cases, it is still independent on the pore structure and dimension. Assuming the core sample as a bundle of capillary channels with same radius, average size of pore throats can be evaluated by Kozeny equation (Kozeny, 1927),

$$d_{th} = (\frac{32k}{\phi})^{1/2} \quad (3)$$

where d_{th} is the average size of pore throat, k and ϕ are the permeability and porosity of the core sample, respectively. The estimated pore throat size is about 4 μm, which is close to the median pore diameter calculated with 4V/A algorithms (5.2 μm) from pore size distribution. It is also in accord with other studies which claims pore throat sizes are normally larger than 2 μm in conventional reservoir rocks (Li et al., 2017; Nelson, 2009). It can also see from the pore size distribution of the core sample (Fig. 2), most pore throat are in the range of 1 to 30 μm with median pore diameter around 13 μm. Therefore, boundaries from Zhang's experiment micromodel (Zhang et al., 2011) (pore throats about 40 μm) is more suitable for interpreting the experimental results than using boundaries proposed by Lenormand's numerical model with pore throats around 230 μm (Lenormand et al., 1988) or by Hu's glass beads model with pore throats about 100 μm (Hu et al., 2020). Based on boundaries proposed by Zhang et al. (2011), CO_2-crude oil displacements are almost situated in viscous force dominated region while CO_2-water displacements are located in capillary force dominated region. It is needed to point out that the Reynolds number ($Re = \frac{\rho v \overline{D_g}}{\mu_d}$, ρ is density of fluid, $\overline{D_g}$ is the median grain size of the porous media, around 100 μm) in this study ranges from about 0.006 to 0.1, indicating that the immiscible displacements were carried out under laminar flow conditions.

Table 3 Summary of Log *Nca* values as a function of injection rate Q.

Defending fluid	Invading fluid	0.05	0.10	0.20	0.30	0.40
		Injection rate Q (mL/min)				
		Log Nca				
crude oil	gCO_2	-5.93	-5.63	-5.33	-5.15	-5.03
crude oil	sCO_2	-5.84	-5.54	-5.24	-5.06	-4.93
crude oil	LCO_2	-5.74	-5.44	-5.14	-4.96	-4.84
water	gCO_2	-7.27	-6.97	-6.67	-6.49	-
water	sCO_2	-7.38	-7.08	-6.78	-6.60	-
water	LCO_2	-7.19	-6.89	-6.59	-6.41	-

3.1 Signatures of differential pressure

In this section, the behaviours of differential pressure are compared between viscous-dominated CO_2-crude oil core flooding and capillary-dominated CO_2-water core flooding. The results have also been demonstrated by pore-scale network experiment as shown in the supporting information.

3.1.1 Differential pressure in viscous dominated displacements

The differential pressures for gCO_2, sCO_2, LCO_2-crude oil displacements are shown in Fig. 7(a)-(c) with injection rate ranging from 0.05 to 0.4 mL/min. The corresponding superficial velocity varies from 2 to 16 μm/s. The inset figure indicates the evolutions of differential pressures before CO_2 breakthrough. The displacements are dominated mainly by viscosity of crude oil and differential pressures are clearly dependent on the injection rates. Before CO_2 breakthrough, differential pressures decrease sharply as CO_2 enters the core sample and pushes out crude oil, resulting in reduction of the length of mobilizable cluster of crude oil (Løvoll et al., 2011; Primkulov et al., 2019). After CO_2 breakthrough, differential pressures vary slightly as most large crude oil cluster are drained out and the effect of viscous force becomes weak. Before CO_2 breakthrough, the viscous differential pressure is almost a linear function of the distance from the outlet to the most advanced front and together with Darcy's law can be estimated as (Løvoll et al., 2011),

$$\Delta P_v = \frac{\mu_d Q}{kA}(L - x_f) \tag{4}$$

where x_f is the position of the most advanced front and L is the length of the core sample. Løvoll et al. (Løvoll et al., 2011) have proposed a relation for the most advanced front position x_f as a function of invading fluid saturation S_{CO2}, capillary number Nca and the length of the system by studying the morphology of the invading cluster in the transition from viscous to capillary fingering and the relation is simplify for the core sample as,

$$x_f = MLS_{CO2}N_{ca}^N \tag{5}$$

where M and N are related to geometry of core sample and can be treated as constant numbers for a sample. The production rate of crude oil can be estimated by the power-law equation (Toth et al., 2002),

$$v(t) = mt^n \tag{6}$$

where t is dimensionless time represented by the injected CO_2 pore volumes, m and n are constant parameters and can be determined through cumulative crude oil production. By assuming CO_2 saturation equals to the production of crude oil, the position of most advanced front can be expressed as,

$$x_f = MLN_{ca}^N \int v(t)dt = \frac{n}{m+1} MLN_{ca}^N t^{m+1} \tag{7}$$

and the viscous dominated differential pressure is,

$$\Delta P_v = \frac{\mu_d QL}{kA}\left(1 - \frac{n}{m+1} MN_{ca}^N t^{m+1}\right) = x(1 - yt^z) \tag{8}$$

where $x = \mu_d QL/kA$, $y = \frac{n}{m+1} MN_{ca}^N$ and $z = m + 1$.

Before CO_2 breakthrough, the differential pressures are well fitted by Eq. (8) with a coefficient of determination (R^2) larger than 0.96, as shown in the inset of Fig. 7. The values of parameter z are indicated in Fig. 8, which is mainly related to the rates of reduction of the pressures. Most of parameter z varies between 0.4 and 0.9 except for two conditions where crude oil was displaced by LCO_2 with an injection rate smaller than 0.1 mL/min (marked in black dash rectangle). These two conditions may fall into the crossover between capillary dominated and viscous dominated regions, agreeing with the phase diagram, which indicates viscous dominated displacements with larger mobility ratio can get into crossover region more easily with a decreasing injection rate. Besides, the value of dimensionless time t is smaller than 1 before CO_2 breakthrough and the differential pressure is as power function of t, which means a greater value of parameter z (larger than 1) will cause smaller variation of the pressure. This is because capillary force becomes considerable and can make up the viscous loss of the pressure when injection rate is decreased.

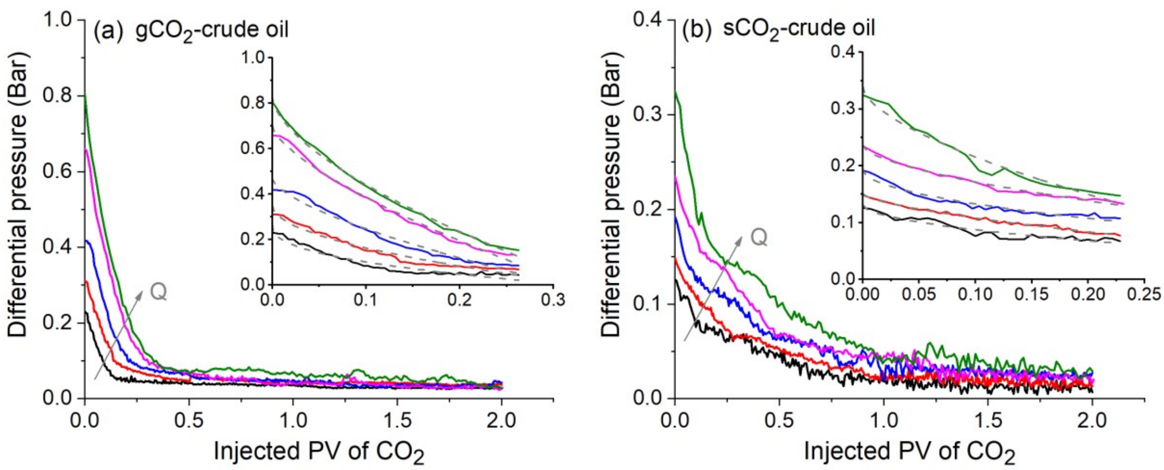

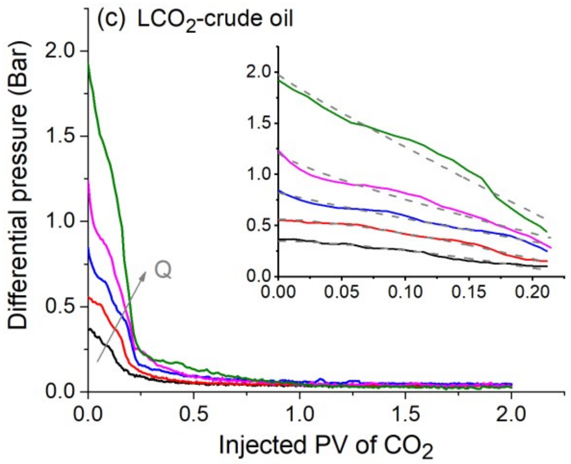

Fig. 7 Differential pressures as a function of injection rate increasing from 0.05 to 0.4 mL/min for (a) gCO_2-crude oil displacement, (b) sCO_2-crude oil displacement and (c) LCO_2-crude oil displacement. The insets showing the differential pressures fitted by Eq. (8) before CO_2 breakthrough (black, red, blue, purple, green curves corresponding to injection flowrate of 0.05, 0.1, 0.2, 0.3 and 0.4 mL/min respectively).

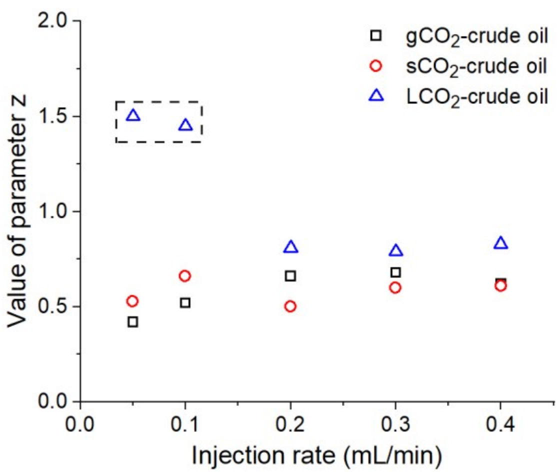

Fig. 8 Value of parameter *z* as a function of injection rate.

3.1.2 Differential pressure in capillary dominated displacements

Fig. 9(a)-(c) show the differential pressures of gCO_2, sCO_2, LCO_2-water displacements with various CO_2 injection rates, which indicates a typical of slow capillary-dominated drainage with intermittent fluctuations (Primkulov et al., 2019). The pressure profiles are all characterized by a jump at the beginning when CO_2 starts to enter the core sample because the pressure in CO_2 needs to be exceed the pressure caused by CO_2-water interfacial tension before its invasion (Cottin et al., 2010). After CO_2 invades the core sample, the pressure in CO_2 increases gradually to overcome the viscous resistance by water and invades the pores with smaller size, leading to the rise of the pressure in fluctuations. And the pressure fluctuations are mostly induced by pore filling events in pore throats, such as Haines jump (Primkulov et al., 2019). At the end of the experiment, the pressure fluctuates around the value of the jump. The value of the pressure jump was observed to be close to the capillary displacement pressure (P_{cd}) derived from the mercury-injection curve by Egermann et al. (Egermann et al., 2006). Fig. 10 indicates the capillary displacement pressure is the largest in gCO_2-water displacement and is almost independent of injection rate. The displacement pressure is resulted from the meniscus formed by the interface between CO_2 and water and it can be described by the Young-Laplace equation (Chalbaud et al., 2007),

$$P_{cd} = \frac{2\sigma_{CO2,w} cos\theta}{R_{throat}^{max}} \tag{9}$$

where $\sigma_{CO2,w}$ is the interfacial tension between CO_2 and water, θ is the contact angle (around 78 ± 7 ° for water), R_{throat}^{max} is the largest connected pore throat. Since the interfacial tension between gCO_2 and water is usually larger than that between sCO_2/LCO_2 and water, the displacement pressure in gCO_2-water displacement is greater than that in sCO_2, LCO_2-water displacement, which is indicated by a more significant jump in the pressure profile. Combining Kozeny equation, Eq. (3), the value of the displacement pressure can be evaluated as,

$$P_{cd} = \frac{\sigma_{CO2,w} cos\theta}{\sqrt{2K/\phi}} \tag{10}$$

The estimated values are 0.077, 0.060 and 0.057 bar for gCO_2, sCO_2, LCO_2-water displacement respectively and they are about 25% larger than the values of displacement pressure from experiments. The reason for the overestimation of displacement pressure is that Kozeny model takes the pore size as uniform for the core sample, which is actually smaller than the size of largest pore throats.

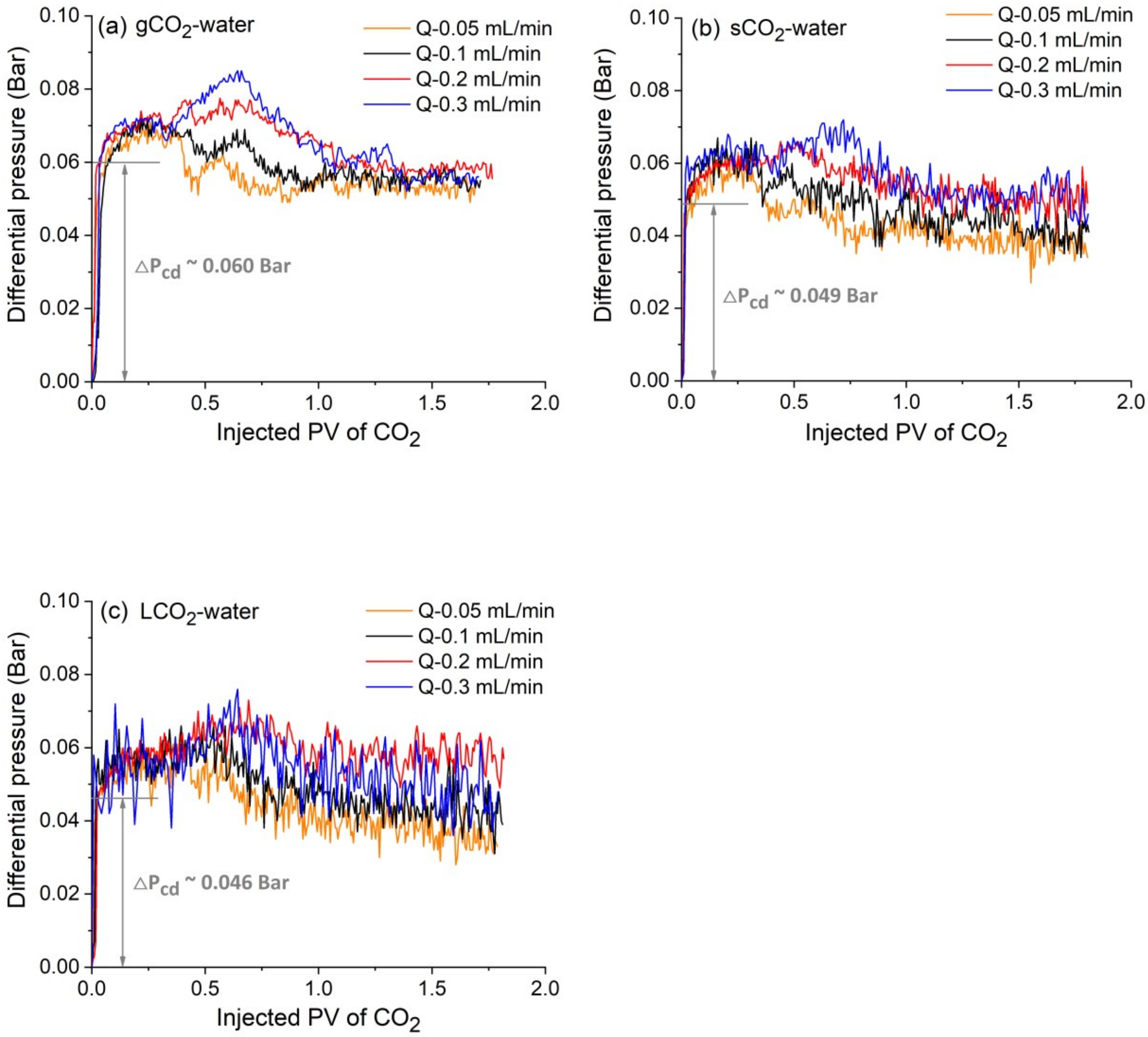

Fig. 9 Differential pressures as a function of injection rate increasing from 0.1 to 0.3 mL/min for (a) gCO_2-water displacement, (b) sCO_2-water displacement and (c) LCO_2-water displacement.

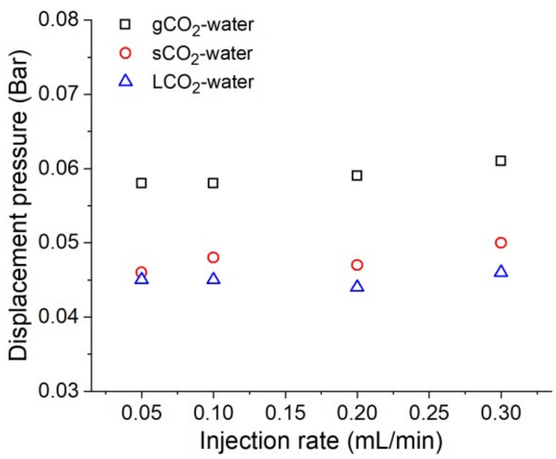

Fig. 10 Displacement pressures for CO_2-water displacements as a function of injection rate.

3.2 Pore-scale perspective of the interplay between capillary and viscous effects

The inlet and outlet pressure are recorded every 6 s in the experiment and this temporal resolution has been proved to be sufficient to capture differences in fluid front configurations by directly imaging pore-scale displacement events in porous rock in real time (Berg et al., 2013). The fluctuations of pressure in the experiment are generally caused by the instability of pump and flow dynamics, like reconfiguration of fluid-fluid interface and variations in effective hydraulic conductance (Aker et al., 1998; Primkulov et al., 2019). To get rid of the influence from pump, pressure fluctuations of CO_2 under different phase states are measured as shown in Fig. S5(a) when the syringe pump is running with constant pressure mode at equilibrium before experiment. Fig. 11(a) shows that the differential pressure profile is split into general trend and pressure fluctuations by using wavelet decomposition (Primkulov et al., 2019; Sygouni et al., 2006) and the values of standard deviation of pressure fluctuations before CO_2 breakthrough are shown in Fig. 11(b). It needs to be pointed out that the results in Fig. 11(b) excludes the pressure fluctuations resulted from instability of pump. In CO_2-water displacements with low *Nca*, the values of pressure fluctuations are almost independent of capillary number and pressure fluctuations are largely dominated by the reconfigurations of the fluid-fluid menisci in pore throats when new pores are invaded (Måløy et al., 1992). The reason for why the differential pressures of CO_2-water displacements fluctuate greatly especially in LCO_2 core flooding is discussed in supporting information (see Fig. S5(b)). In CO_2-crude oil displacements, the values of pressure fluctuations have no relation with capillary number when Log *Nca* is smaller than -5.5 after which they increase obviously with growth of the capillary number and pressure fluctuations are controlled by variation in the effective hydraulic conductance of dominant flow channels (Primkulov et al., 2019).

The reconfiguration of fluid-fluid interface is described by Cieplak-Robbins model in capillary-dominated displacement by introducing three modes of interface advance, burst, touch and overlap (Cieplak and Robbins, 1990). Burst happens most frequently in slow drainage (Singh et al., 2019b; Zhao et al., 2016). Taking pore-scale perspective into consideration, as shown in Fig. 12, to invade a single pore requires overcoming a capillary pressure (P_c) at the pore throat, which is expressed by the general form of Young-Laplace equation,

$$P_c = \sigma(\frac{1}{h} + \frac{1}{a}) \tag{11}$$

where a is the width of pore throat and h is the height. Assuming h is constant, fluctuations of capillary pressure are mainly caused by variation of the width of pore throat a, which yields (Primkulov et al., 2019),

$$\delta P_c \sim \frac{\sigma}{a^2}\delta a \tag{12}$$

Pressure fluctuations in viscous dominated displacements are affected by hydraulic diameter of the channel and the viscous pressure of invading through a pore throat is described by Darcy-Weisbach equation (Primkulov et al., 2019),

$$P_v = \frac{32\mu u l}{h^2}(1 + \frac{h}{a})^2 \tag{13}$$

where u is the flow velocity through the pore throat and l is the distance between two pores. Taking variation of P_v with a obtains,

$$\delta P_v \sim \frac{64\mu u l}{h a^2}(1+\frac{h}{a})\delta a \tag{14}$$

The magnitude of total pressure fluctuations is the sum of δP_v and δP_c, and the ratio of δP_v to δP_c is,

$$\delta P_v/\delta P_c \sim \frac{64\mu u l}{h\sigma}(1+\frac{h}{a}) \sim \frac{64 l}{h}(1+\frac{h}{a})Nca \tag{15}$$

When δP_v and δP_c are comparable, that is, $\delta P_v/\delta P_c \sim 1$, it yields a critical capillary number N_{ca}^*,

$$N_{ca}^* \sim \frac{h}{64 l(1+h/a)} \tag{16}$$

The order of magnitude of pore throat size a is around 1 µm for reservoir core samples (Li et al., 2017) and assume h is comparable to a. The magnitude of l is taken as the same order as the grain size, which is about 100 µm (Pini et al., 2012). The N_{ca}^* is estimated around -4.1 and is a bit different from the critical point (Log *Nca* ~ -5.5) in Fig. 11(b) because the model does not take the effect of wettability and heterogeneity of the porous structure into consideration. This model, however, explains the transition in standard deviation of pressure fluctuations when the displacement is transformed from capillary dominated into viscous dominated.

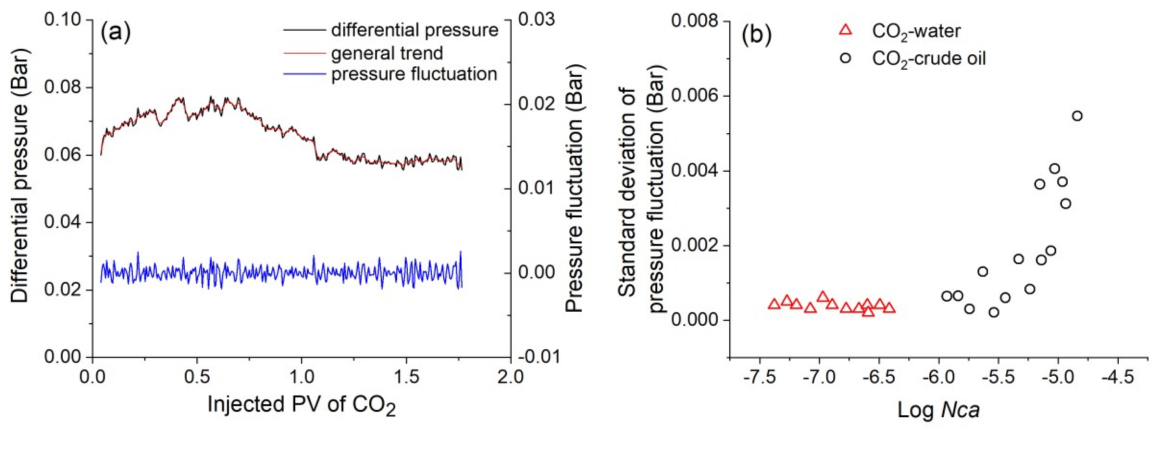

Fig. 11 Wavelet decomposition analysis of the differential pressure: (a) splitting the pressure profile into two components, general trend and fluctuation by taking CO_2-water displacement at an injection rate of 0.2 mL/min as an example and (b) value of standard deviation of pressure fluctuation as a function of Log *Nca*.

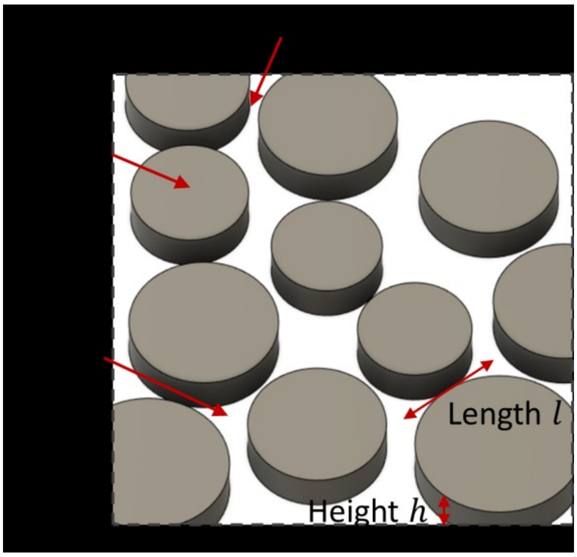

Fig. 12 Pore-scale perspective of two-phase displacement.

3.3 Displacement efficiency

After each experiment, the core sample was taken out from the core holder and was weighed. The residual saturation ($S_{d,res}$) of defending phase thus can be calculated,

$$S_{d,res} = \frac{(m_2 - m_1)/\rho_d}{V_p} \tag{17}$$

Where m_2 is the mass of the core sample after displacement, m_1 is the mass of the dry core sample, ρ_d the density of defending phase and V_p is the pore volume of core sample. The displacement efficiency (η) equals,

$$\eta = 1 - S_{d,res} \tag{18}$$

The relationship between displacement efficiency and Log *Nca* is displayed in Fig. 13. It shows similar trend for water and crude oil displacements. They both exhibit a great increase in displacement efficiency with growing Log *Nca* at smaller Log *Nca* and this growth trend slows down at larger Log *Nca*. In general, the displacement efficiency increases with the increase of Log *Nca* though a small decline appears at the transition from CO_2-water displacement to CO_2-crude oil displacement. For CO_2-water displacement controlled by capillary force, the displacement efficiency grows notably when Log *Nca* is smaller than -6.7 because some water still remains in large pores after drainage with small capillary number and increasing viscous force could overcome the capillary force and push water out. However, it becomes harder to drive more water out at larger capillary number as unrecovered water mainly resides in smaller pores. Further increase in viscous force leads to little production of water (Nobakht et al., 2007). For CO_2-crude oil displacement dominated by viscous force, the rate of increase is obvious when Log *Nca* is smaller than -5.2 since invaded CO_2 is nonwetting and occupies the main channel to push more crude oil out with an increasing injection rate. Besides, formation of additional viscous fingers was observed by increasing viscous force in porous media network (Zhang et al., 2011). It is difficult to displace more crude oil with further increase of viscous force because the remaining crude oil sticks to the surface of the channel due to its affinity to the core sample (Zhao et al., 2016). Interesting to note, a small reduction in displacement efficiency shows in Fig.10 at the crossover from water to crude oil displacement. Similar behaviour also has been found in pore-scale experiment (Wang et al., 2013) and numerical simulation (Lenormand et al., 1988). When the displacement changes from viscous fingering into capillary fingering, the invading phase grows in all directions where the pressure in invade phase is larger than the capillary displacement pressure and more loops are formed as shown in case, leading to an increase in displacement efficiency (An et al., 2020; Wang et al., 2013). This is in accord with the results from pore-scale network by visualization of flow patterns (Fig. S4 in supporting information).

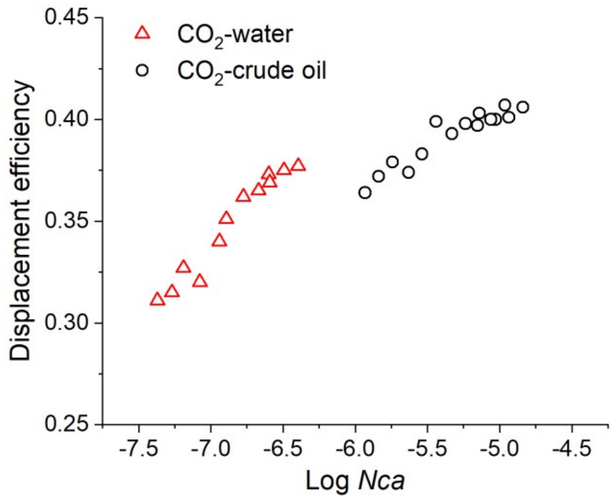

Fig. 13 Displacement efficiency as a function of Log *Nca*.

3.4 Macroscopic capillary number

The aforementioned *Nca* is actually a definition of microscopic capillary number, which is defined at fluid-fluid interface by balancing the viscous stress to the interfacial stress (Leal, 2007). In this definition, the viscous and capillary forces are considered to be equal when *Nca* is around between 10^{-7} and 10^{-5} and the exact value of *Nca* is dependent on the type of tested core sample (Armstrong et al., 2014; Dullien, 2012). This method, therefore, cannot predict the interplay between viscous and capillary forces in a universal condition. The main problem of this definition is that it assumes the viscous and capillary forces act over the same scale and omits the topology of trapped wetting ganglia (Armstrong et al., 2014). In fact, the mobilization of ganglia caused by viscous shear can be extended to many pores ranging up to potentially greater than millimetres and the interfacial stress acts over the length scale of a pore throat which is typically on the order of a few micrometres (Armstrong et al., 2014). Hilfer et al. proposed a macroscopic capillary number N_{ca}^{macro}, which has been shown to correctly describe the mobilization of trapped wetting phase at $N_{ca}^{macro}{\sim}1$ (Hilfer and Oren, 1996). The microscopic and macroscopic capillary number are connected through a rigorous dimensional analysis and defined the macroscopic capillary number as (Hilfer and Oren, 1996),

$$N_{ca}^{macro} = \frac{l_{cl}\mu_d v}{KP_b} = \frac{\sigma l_{cl}}{KP_b} N_{ca} \tag{19}$$

where l_{cl} is the cluster length, consisted of connected mobilizable ganglia and P_b is the breakthrough pressure from the capillary pressure curve, defined as $P_b = P_c(S_w = S_b)$ (Georgiadis et al., 2013; Hilfer and Oren, 1996). The dependence of cluster length on the nature of the sample, fluid properties and experiment conditions can be expressed as $l_{cl} \sim K N_{ca}^{-0.5}/d_{th}$ based on Weitz's study (Weitz et al., 1987). K is the absolute permeability of the core sample and can be treated as constant and the dimensionless cluster length then can be represented as $l_{cl}/d_{th} \sim N_{ca}^{-0.5}$. Fig. 14 shows the data of cluster length from Armstrong et al. (2014) and fitted by the dimensionless cluster length equation $l_{cl}/d_{th} \sim N_{ca}^{-0.5}$. The maximum cluster length in the experiment is restricted by the length of the core sample. Fig. 15(a) shows the macroscopic capillary number calculated using the dimensionless cluster length while Fig. 15(b) presents the macroscopic capillary number calculated by assuming l_{cl} equals to the length of the core sample (L). The values of macroscopic capillary number for CO_2-water displacements are the same and smaller than 1 in these two calculations because they both have the maximum cluster length, L. The values of macro capillary numbers for CO_2-crude oil in these two estimations are a bit different. Assuming l_{cl} equals to the length of the core sample obviously overestimates the macroscopic capillary number especially at larger Log *Nca*. The analysis of macroscopic capillary number further demonstrates that CO_2-water core flooding is capillary-force dominated and CO_2-crude oil displacement is controlled by viscous force. It is also generally in accord with the phase diagram (based on Zhang's boundaries) except few cases of CO_2-crude oil displacements at low injection rates. They are located at the viscous fingering region but with macroscopic capillary number smaller than 1. The main reason for the difference could be the phase diagram was obtained using homogeneous micromodel, but the core sample is heterogeneous, which can be seen from the pore size distribution (Fig. 2).

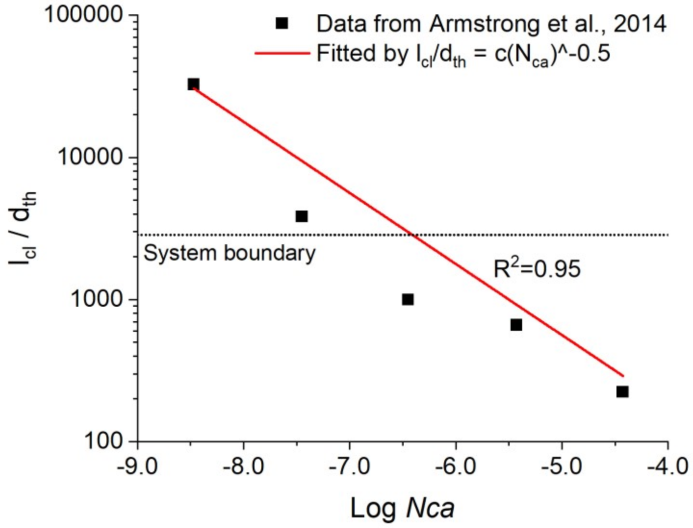

Fig. 14 Data of cluster length from Armstrong et al. (2014) and fitted by the dimensionless cluster length equation.

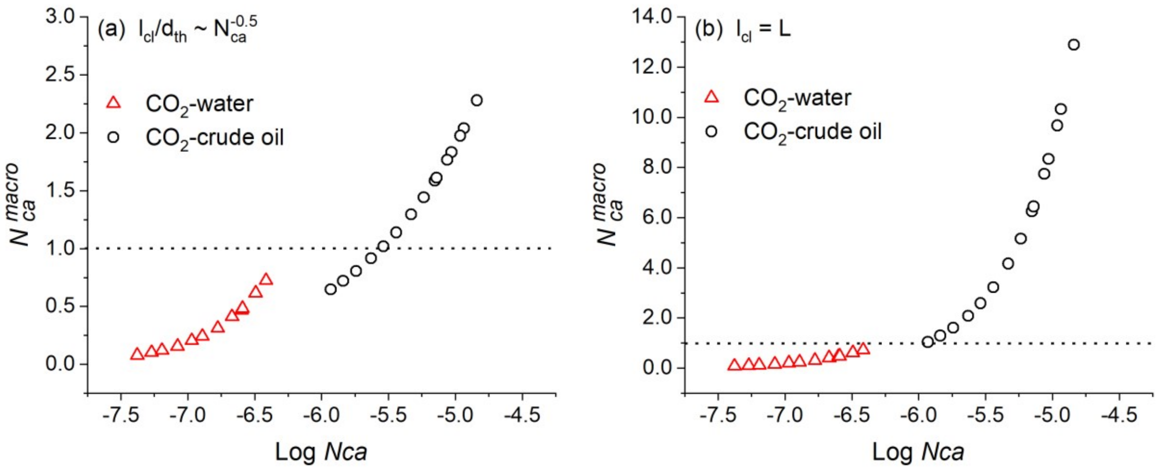

Fig. 15 Macroscopic capillary number calculated using the (a) dimensionless cluster length and (b) length of the core sample *L*.

4. Conclusions

A series of core flooding experiments were conducted to investigate the interplay of capillary and viscous forces in immiscible displacements. Water and crude oil were employed as defending fluid and different states of CO_2 were injected as invading fluid with various injection rates, which obtains a range of capillary numbers and viscosity ratios. The differential pressure in CO_2-crude oil displacement decreases obviously before CO_2 breakthrough and it is well fitted by a power function. The dependency of pressure on the length of mobilizable cluster of crude oil indicates the displacement is governed by the viscosity of crude oil. The exponent of the power function (z) is around 0.4 to 0.9 in most viscous dominated CO_2 flooding, but it becomes significantly larger at the crossover between capillary dominated and viscous dominated regions. The differential pressure in CO_2-water displacement begins with an initial jump, corresponding to the displacement pressure, and then fluctuates around the value of the jump. The displacement pressure evaluated by a modified Young-Laplace equation agrees well with the value of jump from the pressure profiles. The displacement is dominated by the interfacial tension between CO_2 and water. Further analysis of the pressure fluctuations, it is found the value of standard deviation of pressure fluctuations increases with *Nca* in viscous dominated flow but is independent of *Nca* in capillary dominated flow and the transition point is around Log $N_{ca}\sim -5.5$. The displacement efficiency increases with an increasing injection rate both in capillary and viscous dominated displacements and the growth rate slows down at higher *Nca*. The interaction between capillary and viscous effects is verified by macroscopic capillary number with a critical value of $N_{ca}^{macro}\sim 1$, which agrees well with the Log *Nca*-Log *M* phase diagram.

Acknowledgements

Authors gratefully acknowledge the financial supports from China Scholarship Council (CSC) and UK India Education & Research Initiative (UKIERI).

References

Abdul-Majeed, G.H., Al-Soof, N.B.A., 2000. Estimation of gas–oil surface tension. Journal of Petroleum Science and Engineering, 27(3-4): 197-200. DOI:10.1016/S0920-4105(00)00058-9

Abidoye, L.K., Das, D.B., 2020. Impacts of dynamic capillary pressure effects in supercritical CO_2-Water flow: Experiments and numerical simulations. Advances in Water Resources, 136: 103504.

Aker, E., Måløy, K.J., Hansen, A., 1998. Simulating temporal evolution of pressure in two-phase flow in porous media. Physical Review E, 58(2): 2217.

Aker, E., Maloy, K.J., Hansen, A., Basak, S., 2000. Burst dynamics during drainage displacements in porous media: Simulations and experiments. Europhys Lett, 51(1): 55-61. DOI:DOI 10.1209/epl/i2000-00331-2

Amiri, H.A.A., Hamouda, A.A., 2014. Pore-scale modeling of non-isothermal two phase flow in 2D porous media: Influences of viscosity, capillarity, wettability and heterogeneity. International Journal of Multiphase Flow, 61: 14-27. DOI:10.1016/j.ijmultiphaseflow.2014.01.001

An, S., Erfani, H., Godinez‐Brizuela, O.E., Niasar, V., 2020. Transition From Viscous Fingering to Capillary Fingering: Application of GPU‐Based Fully Implicit Dynamic Pore Network Modeling. Water Resources Research, 56(12): e2020WR028149.

Armstrong, R.T., Georgiadis, A., Ott, H., Klemin, D., Berg, S., 2014. Critical capillary number: Desaturation studied with fast X-ray computed microtomography. Geophysical Research Letters, 41(1): 55-60. DOI:10.1002/2013gl058075

Bachu, S., Bennion, D.B., 2008. Interfacial tension between CO_2, freshwater, and brine in the range of pressure from (2 to 27) MPa, temperature from (20 to 125) C, and water salinity from (0 to 334 000) mg· L− 1. Journal of Chemical & Engineering Data, 54(3): 765-775. DOI:10.1021/je800529x

Banner, J., Chatellier, J., Feurer, J., Neuhaus, D., 1992. Guillemot D: a successful appraisal through alternative interpretation. Geological Society, London, Special Publications, 67(1): 129-149. DOI:10.1144/GSL.SP.1992.067.01.06

Berejnov, V., Bazylak, A., Sinton, D., Djilali, N., 2010. Fractal Flow Patterns in Hydrophobic Microfluidic Pore Networks: Experimental Modeling of Two-Phase Flow in Porous Electrodes. J Electrochem Soc, 157(5): B760-B767. DOI:10.1149/1.3332623

Berg, S. et al., 2013. Real-time 3D imaging of Haines jumps in porous media flow. Proc Natl Acad Sci U S A, 110(10): 3755-9. DOI:10.1073/pnas.1221373110

Chalbaud, C.A. et al., 2007. Two Phase Flow Properties of Brine-CO_2 Systems in a Carbonate Core: Influence of Wettability on Pc and kr, SPE/EAGE Reservoir Characterization and Simulation Conference. Society of Petroleum Engineers. DOI:10.2118/111420-MS

Chase Jr, M.W., Tables, N.-J.T., 1998. Data reported in NIST standard reference database 69, June 2005 release: NIST Chemistry WebBook. J. Phys. Chem. Ref. Data, Monograph, 9: 1-1951.

Chen, Y.F., Fang, S., Wu, D.S., Hu, R., 2017. Visualizing and quantifying the crossover from capillary fingering to viscous fingering in a rough fracture. Water Resources Research, 53(9): 7756-7772. DOI:10.1002/2017wr021051

Cieplak, M., Robbins, M.O., 1990. Influence of contact angle on quasistatic fluid invasion of porous media. Phys Rev B Condens Matter, 41(16): 11508-11521. DOI:10.1103/physrevb.41.11508

Cottin, C., Bodiguel, H., Colin, A., 2010. Drainage in two-dimensional porous media: from capillary fingering to viscous flow. Phys Rev E 82(4): 046315. DOI:10.1103/PhysRevE.82.046315

Dullien, F.A., 2012. Porous media: fluid transport and pore structure. Academic press.

Egermann, P., Chalbaud, C.A., Duquerroix, J., Le Gallo, Y., 2006. An integrated approach to parameterize reservoir models for CO_2 injection in aquifers, SPE Annual Technical Conference and Exhibition. Society of Petroleum Engineers. DOI:10.2118/102308-MS

Farokhpoor, R., Bjørkvik, B.J., Lindeberg, E., Torsæter, O., 2013. Wettability behaviour of CO_2 at storage conditions. International Journal of Greenhouse Gas Control, 12: 18-25. DOI:10.1016/j.ijggc.2012.11.003

Furuberg, L., Maloy, K.J., Feder, J., 1996. Intermittent behavior in slow drainage. Phys Rev E Stat Phys Plasmas Fluids Relat Interdiscip Topics, 53(1): 966-977. DOI:10.1103/physreve.53.966

George, H.F., Qureshi, F., 2013. Newton's Law of Viscosity, Newtonian and Non-Newtonian Fluids. In: Wang, Q.J., Chung, Y.-W. (Eds.), Encyclopedia of Tribology. Springer US, Boston, MA, pp. 2416-2420. DOI:10.1007/978-0-387-92897-5_143

Georgiadis, A., Berg, S., Makurat, A., Maitland, G., Ott, H., 2013. Pore-scale micro-computed-tomography imaging: Nonwetting-phase cluster-size distribution during drainage and imbibition. Physical Review E, 88(3): 033002.

Goel, G., Abidoye, L.K., Chahar, B.R., Das, D.B., 2016. Scale dependency of dynamic relative permeability–satuartion curves in relation with fluid viscosity and dynamic capillary pressure effect. Environmental Fluid Mechanics, 16(5): 945-963.

Hilfer, R., Oren, P.E., 1996. Dimensional analysis of pore scale and field scale immiscible displacement. Transport in Porous Media, 22(1): 53-72. DOI:Doi 10.1007/Bf00974311

Holtzman, R., Segre, E., 2015. Wettability Stabilizes Fluid Invasion into Porous Media via Nonlocal, Cooperative Pore Filling. Phys Rev Lett, 115(16): 164501. DOI:10.1103/PhysRevLett.115.164501

Hu, Y., Patmonoaji, A., Zhang, C., Suekane, T., 2020. Experimental study on the displacement patterns and the phase diagram of immiscible fluid displacement in three-dimensional porous media. Advances in Water Resources, 140: 103584.

Johnson, H.D., MacKay, T.A., Stewart, D.J., 1986. The Fulmar Oil-field (Central North Sea): geological aspects of its discovery, appraisal and development. Marine and Petroleum Geology, 3(2): 99-125. DOI:10.1016/0264-8172(86)90023-1

Khudaida, K.J., Das, D.B., 2020. A numerical analysis of the effects of supercritical CO2 injection on CO2 storage capacities of geological formations. Clean Technologies, 2(3): 333-364.

Knudsen, H.A., Hansen, A., 2002. Relation between pressure and fractional flow in two-phase flow in porous media. Physical Review E, 65(5): 056310. DOI:10.1103/PhysRevE.65.056310

Kozeny, J., 1927. Uber kapillare leitung der wasser in boden. Royal Academy of Science, Vienna, Proc. Class I, 136: 271-306.

Leal, L.G., 2007. Advanced transport phenomena: fluid mechanics and convective transport processes, 7. Cambridge University Press.

Leclaire, S., Parmigiani, A., Malaspinas, O., Chopard, B., Latt, J., 2017. Generalized three-dimensional lattice Boltzmann color-gradient method for immiscible two-phase pore-scale imbibition and drainage in porous media. Phys Rev E, 95(3-1): 033306. DOI:10.1103/PhysRevE.95.033306

Lenormand, R., Touboul, E., Zarcone, C., 1988. Numerical-Models and Experiments on Immiscible Displacements in Porous-Media. Journal of Fluid Mechanics, 189: 165-187. DOI:Doi 10.1017/S0022112088000953

Li, H.G., Li, H.M., Gao, B.B., Wang, W., Liu, C., 2017. Study on pore characteristics and microstructure of sandstones with different grain sizes. J Appl Geophys, 136: 364-371. DOI:10.1016/j.jappgeo.2016.11.015

Li, Y., Yu, Q., 2020. Rock-core scale modeling of initial water saturation effects on CO2 breakthrough pressure in CO2 geo-sequestration. Journal of Hydrology, 580: 124234. DOI:10.1016/j.jhydrol.2019.124234

Løvoll, G. et al., 2011. Influence of viscous fingering on dynamic saturation–pressure curves in porous media. Transport in porous media, 86(1): 305-324. DOI:10.1007/s11242-010-9622-8

Måløy, K.J., Feder, J., Jøssang, T.J.P.r.l., 1985. Viscous fingering fractals in porous media. Physical review letters, 55(24): 2688. DOI:10.1103/PhysRevLett.55.2688

Måløy, K.J., Furuberg, L., Feder, J., Jøssang, T.J.P.r.l., 1992. Dynamics of slow drainage in porous media. Physical review letters, 68(14): 2161. DOI:10.1103/PhysRevLett.68.2161

Messaadi, A. et al., 2015. A New Equation Relating the Viscosity Arrhenius Temperature and the Activation Energy for Some Newtonian Classical Solvents. Journal of Chemistry, 2015. DOI:10.1155/2015/163262

Nelson, P.H., 2009. Pore-throat sizes in sandstones, tight sandstones, and shales. Aapg Bulletin, 93(3): 329-340. DOI:10.1306/10240808059

Nobakht, M., Moghadarn, S., Go, Y., 2007. Effects of viscous and capillary forces on CO2 enhanced oil recovery under reservoir conditions. Energy & Fuels, 21(6): 3469-3476. DOI:10.1021/ef700388a

Patmonoaji, A., Muharrik, M., Hu, Y., Zhang, C., Suekane, T., 2020. Three-dimensional fingering structures in immiscible flow at the crossover from viscous to capillary fingering. International Journal of Multiphase Flow, 122: 103147.

Pini, R., Krevor, S.C.M., Benson, S.M., 2012. Capillary pressure and heterogeneity for the CO2/water system in sandstone rocks at reservoir conditions. Advances in Water Resources, 38: 48-59. DOI:10.1016/j.advwatres.2011.12.007

Primkulov, B.K. et al., 2019. Signatures of fluid-fluid displacement in porous media: wettability, patterns and pressures. Journal of Fluid Mechanics, 875. DOI:10.1017/jfm.2019.554

Singh, K., Bultreys, T., Raeini, A.Q., Shams, M., Blunt, M.J., 2019a. Imbibition in porous media: correlations of displacement events with pore-throat geometry and the identification of a new type of pore snap-off. doi:10.31223/osf.io/62gfr.

Singh, K., Jung, M., Brinkmann, M., Seemann, R., 2019b. Capillary-Dominated Fluid Displacement in Porous Media. Annual Review of Fluid Mechanics, 51: 429-449. DOI:10.1146/annurev-fluid-010518-040342

Sygouni, V., Tsakiroglou, C.D., Payatakes, A.C.J.P.o.F., 2006. Capillary pressure spectrometry: Toward a new method for the measurement of the fractional wettability of porous media. Physics of Fluids 18(5): 053302. DOI:10.1063/1.2203667

Toth, J., Bodi, T., Szucs, P., Civan, F., 2002. Convenient formulae for determination of relative permeability from unsteady-state fluid displacements in core plugs. Journal of Petroleum Science and Engineering, 36(1-2): 33-44. DOI:10.1016/S0920-4105(02)00249-8

Tsuji, T., Jiang, F., Christensen, K.T., 2016. Characterization of immiscible fluid displacement processes with various capillary numbers and viscosity ratios in 3D natural sandstone. Advances in Water Resources, 95: 3-15. DOI:10.1016/j.advwatres.2016.03.005

Wang, Y. et al., 2013. Experimental study of crossover from capillary to viscous fingering for supercritical CO2–water displacement in a homogeneous pore network. Environmental science & technology, 47(1): 212-218. DOI:10.1021/es3014503

Weitz, D.A., Stokes, J.P., Ball, R.C., Kushnick, A.P., 1987. Dynamic capillary pressure in porous media: Origin of the viscous-fingering length scale. Phys Rev Lett, 59(26): 2967-2970. DOI:10.1103/PhysRevLett.59.2967

Yamabe, H., Tsuji, T., Liang, Y., Matsuoka, T.J.E.s., technology, 2015. Lattice Boltzmann simulations of supercritical CO2–water drainage displacement in porous media: CO2 saturation and displacement mechanism. Environmental science & technology, 49(1): 537-543. DOI:10.1021/es504510y

Zacharoudiou, I., Boek, E.S., Crawshaw, J.J.S.r., 2018. The impact of drainage displacement patterns and Haines jumps on CO2 storage efficiency. Scientific reports, 8(1): 15561. DOI:10.1038/s41598-018-33502-y

Zhang, C.Y., Oostrom, M., Wietsma, T.W., Grate, J.W., Warner, M.G., 2011. Influence of Viscous and Capillary Forces on Immiscible Fluid Displacement: Pore-Scale Experimental Study in a Water-Wet Micromodel Demonstrating Viscous and Capillary Fingering. Energy & Fuels, 25(8): 3493-3505. DOI:10.1021/ef101732k

Zhao, B., MacMinn, C.W., Juanes, R., 2016. Wettability control on multiphase flow in patterned microfluidics. Proc Natl Acad Sci U S A, 113(37): 10251-6. DOI:10.1073/pnas.1603387113

Zhou, X. et al., 2020. Evaluation of enhanced oil recovery potential using gas/water flooding in a tight oil reservoir. Fuel, 272: 117706. DOI:10.1016/j.fuel.2020.117706